arXiv:2505.03191v1 [cond-mat.mes-hall] 6 May 2025

Photocurrent generation from spin dynamics in antiferromagnetic Dirac semimetals

Kohei Hattori,[1,*] Hikaru Watanabe,[2,†] and Ryotaro Arita[2,3]

[1] *Department of Applied Physics, The University of Tokyo, Bunkyo, Tokyo 113-8656, Japan*
[2] *Department of Physics, University of Tokyo, Hongo, Tokyo 113-0033, Japan*
[3] *Center for Emergent Matter Science, RIKEN, Wako, Saitama 351-0198, Japan*

Using real-time simulations, we explore the photocurrent induced by localized spin dynamics in antiferromagnetic Dirac semimetals. These materials exhibit strong spin-charge coupling because the energy scales of the electronic and spin systems are of the same order. The photocurrent response exhibits a pronounced peak reflecting the presence of the Dirac point at the resonance frequency of the localized spin system. This contribution plays a crucial role in the photocurrent generation when the electronic filling is set around the Dirac nodes in the Dirac semimetal. We also reveal that the photocurrent response exhibits a low-frequency divergence due to the modulation of the resonance frequency of the localized spin system. Our findings clarify that the photocurrent response arising from the spin dynamics reflects the band topology of the Dirac semimetals, and the localized spin dynamics plays an important role in the photocurrent generation.

Introduction— The photocurrent response is a second-order current response that converts an oscillating light field into a direct current (DC) [1–3]. In topological semimetals, the property of the photocurrent response driven by the external electric field reflects the topology of the band structure [4, 5]. In Weyl semimetals, the injection current induced by circularly polarized light in the low-frequency regime is shown to be quantized due to the presence of Weyl charges [6, 7]. Moreover, the amplitude of the photocurrent response in topological semimetals is proposed to exhibit a divergent behavior in the low-frequency regime [8–12]. In experiments, the large photocurrent generation is observed in topological semimetals in the low-frequency regime [13–15].

In recent years, photocurrent generation driven by order parameter dynamics has attracted significant attention. In the low-frequency regime, collective excitations of order parameters modify the photocurrent response. The influence of order parameter dynamics on photocurrent response has been investigated through perturbative analysis [16–20] and real-time simulations [21–24] theoretically. Experimentally, photocurrent responses originating from order parameter dynamics have been observed in excitonic insulators [25–27], ferroelectrics [28], and magnetic insulators [29]. Photocurrent generation driven by the order parameter dynamics in the low-frequency regime is expected to reflect the band topology in a topological semimetal.

On the other hand, there has been growing interest in electric control of antiferromagnetic order in light of spintronic applications [30–32]. In noncentrosymmetric AFMs, localized spin dynamics can be driven by an electric field through linear magnetoelectric effects and the Edelstein effect [33–36]. Experimentally, electrical switching of AFM domains has been demonstrated in the AFM Dirac semimetal CuMnAs [37, 38]. In AFM Dirac semimetals, localized spin dynamics is expected to play a crucial role in photocurrent generation owing to the comparable energy scales of the electronic and localized spin systems.

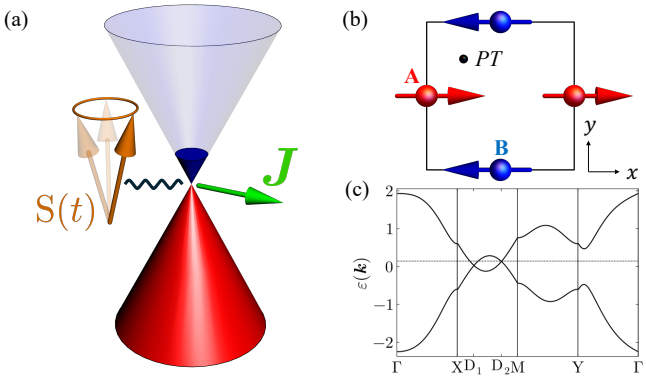

FIG. 1. (a) Schematic picture of photocurrent arising from localized spin dynamics in Dirac semimetals. Through the exchange coupling between the electronic spin moment and the localized spin moment, the localized spin dynamics $\mathrm{S}(t)$ generates the photocurrent response $\boldsymbol{J}$. (b) Picture of collinear AFM order. The black dot represents the $\mathcal{PT}$-symmetry center. (c) Band dispersion of the system when $t_1 = 1.0, t_2 = 0.08, \alpha = 0.8, J = 0.6$. $\mathrm{D}_1, \mathrm{D}_2$ represent the Dirac points.

In this work, we investigate the behavior of the photocurrent response, especially the injection current induced by localized spin dynamics in AFM Dirac semimetals. To calculate the photocurrent generation from the localized spin dynamics, we perform real-time simulations of the Kondo lattice model, following previous studies [23, 24, 39–41]. Using this approach, we analyze the chemical potential dependence (μ-dependence) of the photocurrent conductivity and examine its behavior in the low-frequency regime. We reveal that the photocurrent response arising from the localized spin dynamics exhibits a single peak reflecting the presence of the Dirac point, which is absent in the electric field-driven photocurrent. We also find that the photocurrent generation from the spin dynamics shows divergent behavior in the low-frequency regime. Our findings reveal that the pho-

tocurrent driven by the localized spin dynamics reflects the topology of the Dirac dispersion in the AFM Dirac semimetal.

Model and method— We evaluate the photocurrent generation from localized spin dynamics in parity-time-reversal symmetric ($\mathcal{PT}$-symmetric) collinear AFM Dirac semimetal (see FIG. 1(a)) by real-time simulation following Ref. cite hattori2025. First, we consider the minimal model of the AFM Dirac semimetals on the two-dimensional square lattice introduced in Ref [42]. The schematic picture of the system is illustrated in FIG. 1(b). We can divide the Hamiltonian of this model into four parts as $\mathcal{H} = \hat{\mathcal{H}}_{\rm ele} + \hat{\mathcal{H}}_{\rm exc} + \mathcal{H}_{\rm mag} + \hat{\mathcal{H}}_E$. The first term, $\hat{\mathcal{H}}_{\rm ele} = \sum_{\boldsymbol{k}} \hat{\boldsymbol{c}}^\dagger(\boldsymbol{k})\boldsymbol{\mathcal{H}}_{\rm ele}(\boldsymbol{k})\hat{\boldsymbol{c}}(\boldsymbol{k})$ represents the electronic Hamiltonian, where $\hat{\boldsymbol{c}}(\boldsymbol{k}) = (\hat{c}_{A\uparrow}(\boldsymbol{k}), \hat{c}_{A\downarrow}(\boldsymbol{k}), \hat{c}_{B\uparrow}(\boldsymbol{k}), \hat{c}_{B\downarrow}(\boldsymbol{k}))^T$is a vector of annihilation operators of the electron labeled by sublattice index α ($\alpha = A, B$), spin σ ($\sigma =\uparrow,\downarrow$), and wave vector $\boldsymbol{k}$. The matrix of the Hamiltonian is expressed as

$$\boldsymbol{\mathcal{H}}_{\rm ele}(\boldsymbol{k}) = -2t_1\tau^x \cos\frac{k_x}{2}\cos\frac{k_y}{2} - t_2(\cos k_x + \cos k_y) + \lambda\tau_z(\sigma_y \sin k_x - \sigma_x \sin k_y), \tag{1}$$

where $t_1(t_2)$ is the nearest-neighbor hopping (next-nearest-neighbor hopping), and λ is the staggard spin-orbit coupling. Here, the Pauli matrices $\sigma(\tau)$ represent the spin (sublattice) degree of freedom. The second term, $\hat{\mathcal{H}}_{\rm exc} = \sum_{\boldsymbol{k}} \hat{\boldsymbol{c}}^\dagger(\boldsymbol{k})\boldsymbol{\mathcal{H}}_{\rm exc}(\boldsymbol{k})\hat{\boldsymbol{c}}(\boldsymbol{k})$, represents the interaction between the electronic system and localized spin system, where the matrix is expressed as

$$\boldsymbol{\mathcal{H}}_{\rm exc}(\boldsymbol{k}) = J\left[\frac{1+\tau_z}{2}\boldsymbol{\sigma}\cdot \mathrm{S}_A + \frac{1-\tau_z}{2}\boldsymbol{\sigma}\cdot \mathrm{S}_B\right]. \tag{2}$$

Here, J represents the exchange coupling between the electronic spin moment $\boldsymbol{\sigma}_\alpha$ and the localized spin moment S_α on the sublattice site α. The third term, $\mathcal{H}_{\rm spin} = \sum_{\alpha=\mathrm{A,B}} K_x(\mathrm{S}^x_\alpha)^2$, corresponds to the spin Hamiltonian, where K_x is the coefficient of the easy-axis anisotropy along the x-axis. The last term $\hat{\mathcal{H}}_E = -\boldsymbol{E}(t)\sum_{\boldsymbol{k}\boldsymbol{k}'} \hat{\boldsymbol{c}}^\dagger(\boldsymbol{k})\left[i\frac{\partial}{\partial \boldsymbol{k}}\delta(\boldsymbol{k}-\boldsymbol{k}')\right]\hat{\boldsymbol{c}}(\boldsymbol{k}')$ is the light-matter coupling in the length gauge [43], where $\boldsymbol{E}(t)$ represents the external light field.

In this study, we consider the collinear AFM order $\mathrm{S}_A = -\mathrm{S}_B = (1,0,0)$ and the electronic Hamiltonian $\hat{\mathcal{H}}_{\rm ele} + \hat{\mathcal{H}}_{\rm exc}$ can be diagonalized analytically as

$$E_{\boldsymbol{k}\pm} = -t_2(\cos k_x + \cos k_y) \pm \left[4t_1^2\cos^2\frac{k_x}{2}\cos^2\frac{k_y}{2} + (J-\lambda\sin k_y)^2 + \lambda^2\sin^2 k_x\right]^{1/2}. \tag{3}$$

Here, we set the parameters as $t_1 = 1.0, t_2 = 0.08, \lambda = 0.8, J = 0.6$ and the Dirac points appear at k-points $\mathrm{D}_1 = [\pi, \arccos(J/\lambda)], \mathrm{D}_2 = [\pi, \pi - \arccos(J/\lambda)]$ in the band diagram (FIG. 1(c)). We define the energy of the lower (upper) Dirac point by μ_1 (μ_2). These Dirac points are protected by the nonsymmorphic mirror symmetry [42, 44].

To compute both electronic dynamics and spin dynamics, we solve the two-coupled equations of motion, the von Neumann equation and the Landau-Lifshitz-Gilbert (LLG) equation. For the electronic system, we solve the von Neumann equation [45] for the single-particle density matrix (SPDM) $\rho^{\sigma\sigma'}_{\alpha\beta}(\boldsymbol{k}) = \left\langle \hat{c}^\dagger_{\beta\sigma'}(\boldsymbol{k})\hat{c}_{\alpha\sigma}(\boldsymbol{k})\right\rangle$ expressed as

$$\frac{\partial \boldsymbol{\rho}(\boldsymbol{k},t)}{\partial t} = -i[\boldsymbol{H}(\boldsymbol{k},t),\, \boldsymbol{\rho}(\boldsymbol{k},t)] - \boldsymbol{E}(t)\cdot\frac{\partial \boldsymbol{\rho}(\boldsymbol{k},t)}{\partial \boldsymbol{k}} - \frac{1}{\tau}(\boldsymbol{\rho}(\boldsymbol{k},t) - \boldsymbol{\rho}_{\rm eq}(\boldsymbol{k})). \tag{4}$$

Here, τ is the relaxation time of the electronic system and $\boldsymbol{H}(\boldsymbol{k},t)$ is the time-dependent electronic Hamiltonian at each $\boldsymbol{k}$ point defined as $\hat{\mathcal{H}}_{\rm ele} + \hat{\mathcal{H}}_{\rm exc} = \sum_{\boldsymbol{k}} \hat{\boldsymbol{c}}^\dagger(\boldsymbol{k})\boldsymbol{H}(\boldsymbol{k},t)\hat{\boldsymbol{c}}(\boldsymbol{k})$.

On the other hand, we solve the LLG equation for the localized spin moment S_α described as

$$\frac{d\mathbf{S}_\alpha}{dt} = \frac{1}{1+\alpha_G^2}\left(\mathbf{h}^{\rm eff}_\alpha \times \mathbf{S}_\alpha + \alpha_G \mathbf{S}_\alpha \times \left(\mathbf{S}_\alpha \times \mathbf{h}^{\rm eff}_\alpha\right)\right), \tag{5}$$

where $\mathbf{h}^{\rm eff}_\alpha = -J\langle\boldsymbol{\sigma}_\alpha\rangle + \frac{\delta\mathcal{H}_{\rm spin}}{\delta\mathbf{S}_\alpha}$ is the effective magnetic field on the localized spin moment on the sublattice α and α_G is the Gilbert damping coefficient. In the following calculation, we set the k-mesh of the Brillouin zone to 1000×1000, and use $\tau = 100$, $\alpha_G = 0.01$, and inverse temperature $\beta = 500.0$.

Response functions— Here, we discuss response functions, specifically linear electromagnetic susceptibility and photocurrent conductivity. In this section, we use $\mu = \mu_2 + 0.05$ and $K_x = 0.1$. For this parameter, the peak structure of the photocurrent conductivity arising from the electric field does not appear at the resonance frequency of the localized spin system. First, we calculate the linear electromagnetic susceptibility of the localized spins. We define the symmetry-adapted basis for the localized spin system as $\mathrm{M}^a(t) = \frac{1}{2}(\mathrm{S}^a_A(t) + \mathrm{S}^a_B(t)), \mathrm{L}^a(t) = \frac{1}{2}(\mathrm{S}^a_A(t) - \mathrm{S}^a_B(t))$, where $\mathrm{M}^a(t)$ represents the ferroic magnetization and $\mathrm{L}^a(t)$ means the staggered spin moments. For these symmetry-adapted bases, we calculate the linear electromagnetic susceptibility defined as

$$\chi_{\mathrm{S}^\mu E^\nu}(\omega) = \frac{\Delta\mathrm{S}^\mu(\omega)}{E^\nu(\omega)}, \tag{6}$$

where $\Delta\mathrm{S}^\mu(\omega)$ is the Fourier component of the modulation of the symmetry-adapted basis $\Delta\mathrm{M}^a(t) = \mathrm{M}^a(t) - \mathrm{M}^a(0), \Delta\mathrm{L}^a(t) = \mathrm{L}^a(t) - \mathrm{L}^a(0)$, and $E^\nu(\omega)$ is the Fourier component of the external light field along the ν-axis. Considering the symmetry analysis of the symmetry-adapted basis in Supplemental Materials (SM) [46], only L^y and M^z are optically active in the linear response

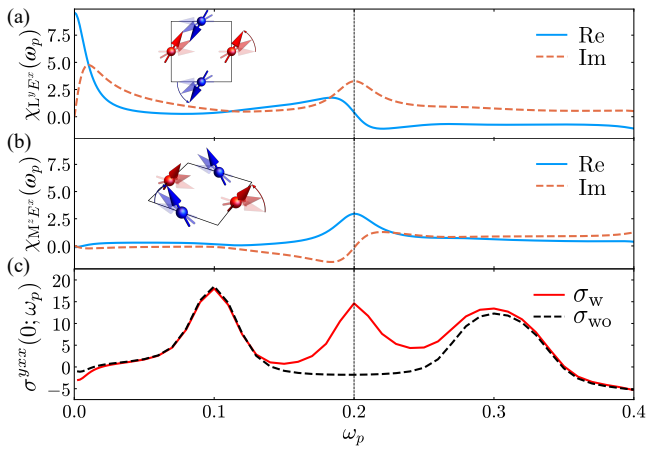

FIG. 2. (a),(b) Linear electromagnetic susceptibility of symmetry-adapted basis L^y and M^z when $\tau = 100$. The blue solid line (orange dashed line) shows the real part (imaginary part) of the linear electromagnetic susceptibility. (c) Transverse photocurrent conductivity $\sigma^{yxx}(0;\omega_{\rm p})$ when $\tau = 100$. The red solid line (black dashed line) corresponds to the photocurrent conductivity with the effect of localized spin dynamics (without the effect of localized spin dynamics). The vertical dotted line shows the resonance frequency of the localized spin system ($\omega_{\rm p} = 0.2$).

regime. We present the frequency dependence of the linear electromagnetic susceptibility for the symmetry-adapted bases L^y and M^z in FIG. 2(a) and (b). The electromagnetic susceptibilities $\chi_{\mathrm{L}^y E^x}(\omega_{\rm p})$ and $\chi_{\mathrm{M}^z E^x}(\omega_{\rm p})$ exhibit distinct peak structures at $\omega_{\rm p} = 0.2$, which correspond to the collective excitations of the localized spin system.

Next, we discuss the transverse photocurrent response described as

$$J^y(\omega = 0;\omega_{\rm p}) = \sigma^{yxx}(0;-\omega_{\rm p},\omega_{\rm p})E^x(-\omega_{\rm p})E^x(\omega_{\rm p}) + \sigma^{yxx}(0;\omega_{\rm p},-\omega_{\rm p})E^x(\omega_{\rm p})E^x(-\omega_{\rm p}), \quad (7)$$

where $J^y(\omega = 0;\omega_{\rm p})$ is the DC component of the current response under the external electric field with frequency $\omega_{\rm p}$. We define the photocurrent conductivity as $\sigma^{yxx}(0;\omega_{\rm p}) = (\sigma^{yxx}(0;-\omega_{\rm p},\omega_{\rm p}) + \sigma^{yxx}(0;\omega_{\rm p},-\omega_{\rm p}))/2$ in this study. Here, we show the frequency dependence of the photocurrent conductivity with the effect of spin dynamics $\sigma_{\rm w}(0;\omega_{\rm p})$ and without the effect of spin dynamics $\sigma_{\rm wo}(0;\omega_{\rm p})$ in FIG. 2(c). The two peak structures at $\omega_{\rm p} = 0.1, 0.3$ in $\sigma_{\rm wo}(0;\omega_{\rm p})$ correspond to the electronic excitation around the two Dirac nodes. Considering the effect of the localized spin dynamics, we observe the strong enhancement of the photocurrent conductivity around the resonance frequency $\omega_{\rm p} = 0.2$ in $\sigma_{\rm w}(0;\omega_{\rm p})$, which arises from the collective excitation of the localized spin system. This behavior is unique to narrow optical gap systems, where the energy scale of the localized spin system is comparable to that of the electronic system.

Chemical potential dependence— We discuss the μ-

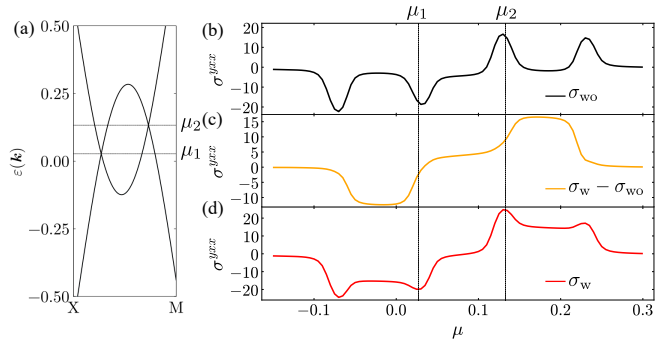

FIG. 3. μ-dependence of photocurrent conductivity at resonance frequency $\omega_{\rm p} = 0.2$ when $\tau = 100$. (a) Band dispersion around Dirac nodes along X-M line. The chemical potential μ_1 (μ_2) corresponds to the energy at the lower (upper) Dirac point. (b),(c),(d) μ-dependence of $\sigma_{\rm wo}(0,\omega_{\rm p} = 0.2)$, $\sigma_{\rm w}(0,\omega_{\rm p} = 0.2) - \sigma_{\rm wo}(0,\omega_{\rm p} = 0.2)$ and $\sigma_{\rm w}(0,\omega_{\rm p} = 0.2)$. The chemical potentials μ_1 and μ_2 represented by the horizontal dotted lines in (a) correspond to the three vertical dotted lines in (b),(c), and (d).

dependence of the photocurrent response in the Dirac semimetal. Let us focus on the injection current term involved in the photocurrent conductivity. The formula for the injection current is given by

$$J^{\mu;\nu\lambda}_{XY;\mathrm{Inj}}(0,\omega_{\rm p}) = \sigma^{\mu;\nu\lambda}_{XY;\mathrm{Inj}}(0;-\omega_{\rm p},\omega_{\rm p})X^\nu(-\omega_{\rm p})Y^\lambda(\omega_{\rm p}) + \sigma^{\mu;\nu\lambda}_{XY;\mathrm{Inj}}(0;\omega_{\rm p},-\omega_{\rm p})X^\nu(\omega_{\rm p})Y^\lambda(-\omega_{\rm p}) \quad (8)$$

where $X^\nu(\omega_{\rm p})$ and $Y^\lambda(\omega_{\rm p})$ correspond to the external fields such as the electric field or the localized spin dynamics with frequency $\omega_{\rm p}$. When $X^\mu(\omega_{\rm p})$ is the localized spin dynamics driven by the external light field, we can express the localized spin dynamics as

$$X^\mu(\omega_{\rm p}) = \chi_{X^\mu E^\nu}(\omega_{\rm p})E^\nu(\omega_{\rm p}), \quad (9)$$

where $\chi_{\mathrm{X}^\mu E^\nu}(\omega_{\rm p})$ is the electromagnetic susceptibility of X^μ. The general formula for the injection current conductivity $\sigma^{\mu;\nu\lambda}_{XY;\mathrm{Inj}}(0;-\omega_{\rm p},\omega_{\rm p})$ in Eq. (8) is expressed as

$$\sigma^{\mu;\nu\lambda}_{XY;\mathrm{Inj}}(0;-\omega_{\rm p},\omega_{\rm p}) = \pi\tau\int\frac{d\boldsymbol{k}}{(2\pi)^d}\sum_{a\neq b}\Delta^\mu_{ab}X^\nu_{ab}Y^\lambda_{ba}f_{ab}\delta(\omega_{\rm p}-\epsilon_{ba}), \quad (10)$$

where $\Delta^\mu_{ab} = \partial_\mu(\epsilon_{a\boldsymbol{k}} - \epsilon_{b\boldsymbol{k}})$ is the velocity difference matrix, and $X^\nu_{ab}, Y^\lambda_{ba}$ represent the matrix element of either the Berry connection, $\boldsymbol{\xi}_{ab} = i\langle u_{a\boldsymbol{k}}|\nabla_{\boldsymbol{k}}|u_{b\boldsymbol{k}}\rangle$, or the spin operator $\boldsymbol{\sigma}_{ab}$ in the band basis $|u_{n\boldsymbol{k}}\rangle$, where the eigenstates are characterized by the energy $\epsilon_{n\boldsymbol{k}}$ and momentum $\boldsymbol{k}$. The quantity $f_{ab} = f_a - f_b$ denotes the difference in the Fermi distribution function, where $f_a = f(\epsilon_{a\boldsymbol{k}})$, and $\epsilon_{ba} = \epsilon_{b\boldsymbol{k}} - \epsilon_{a\boldsymbol{k}}$ represents the energy difference between bands a and b. Notably, the injection current is linearly proportional to the relaxation time, and

$\tau = 100$ is sufficiently large for the injection currents to dominate the photocurrent conductivity in the finite-frequency regime. Under these conditions, we discuss the μ-dependence of the injection current through real-time simulation.

We present the μ-dependence of the total photocurrent conductivity $\sigma_{\rm wo}(0;\omega_{\rm p})$, $\sigma_{\rm w}(0;\omega_{\rm p})-\sigma_{\rm wo}(0;\omega_{\rm p})$, and $\sigma_{\rm w}(0;\omega_{\rm p})$, at the resonance frequency $\omega_{\rm p}=0.2$ in FIG. 3. We show the band diagram around the two Dirac nodes in FIG. 3(a), and the chemical potentials μ_1 and μ_2 correspond to the energy at the lower Dirac point and upper Dirac point. In FIG. 3(b), $\sigma_{\rm wo}(0;\omega_{\rm p})$ exhibits four peaks around the Dirac points, and this peak structure corresponds to that of the injection current induced by linearly polarized light, which features a double-peak structure around the Dirac point. We also observe the pronounced dip structures around $\mu=-0.05$ and $\mu=0.2$ in the μ-dependence of $\sigma_{\rm wo}(0;\omega_{\rm p})$. The width of these dip structures is determined by the energy gap $\mu_1-\mu_2$ between the two Dirac points. In contrast, the photocurrent component involving localized spin dynamics, $\sigma_{\rm w}(0;\omega_{\rm p})-\sigma_{\rm wo}(0;\omega_{\rm p})$, has the two peak structures separated by the energy difference $\mu_1-\mu_2$ between the two Dirac points in FIG. 3(c). This behavior is similar to that of the injection current induced by circularly polarized light, which exhibits a single peak at the degenerate point with a value quantized by a physical constant [6, 7]. The circular injection-like behavior cannot arise solely from the electric field effect in a $\mathcal{PT}$-symmetric magnet. We confirm that the localized spin dynamics can give rise to the circular injection current-like behavior reflecting the presence of the Dirac point by using the analytical formula for the injection current of the effective Dirac Hamiltonian, as detailed in the SM [46]. As a result, in the μ-dependence of $\sigma_{\rm w}(0;\omega_{\rm p})$, which incorporates the influence of spin dynamics, the dip structure in $\sigma_{\rm wo}(0;\omega_{\rm p})$ is compensated by the photocurrent contributions from localized spin dynamics, $\sigma_{\rm w}(0;\omega_{\rm p})-\sigma_{\rm wo}(0;\omega_{\rm p})$ in FIG. 3(d). Consequently, the localized spin dynamics plays an important role in the generation of a substantial photocurrent response under linearly polarized light when the electronic filling is set around the Dirac nodes.

Low-frequency divergence— Here, we discuss the low-frequency divergence of the photocurrent response arising from the localized spin dynamics. In the conventional theory [9, 10], the low-frequency divergence of the photocurrent occurs as the chemical potential approaches the Dirac point. In contrast, the low-frequency divergence of photocurrent generation driven by the spin dynamics arises from tuning the resonance frequency of the localized spin system. In this model, we can modify the resonance frequency of the localized spin system by changing the value of the easy-axis anisotropy K_x. We note that the electronic band structure does not depend on K_x because the magnetic anisotropy along the x-axis does not modulate the localized spin configuration.

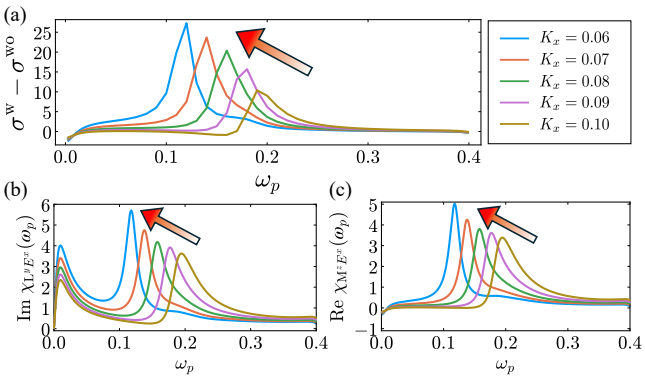

FIG. 4. (a) Low-frequency divergence of photocurrent generation from localized spin dynamics $\sigma_{\rm w}(0;\omega_{\rm p})-\sigma_{\rm wo}(0;\omega_{\rm p})$. (b),(c) Magnetic anisotropy dependence of the linear electromagnetic susceptibility $\chi_{{\rm L}^y E^x}(\omega_{\rm p})$ and $\chi_{{\rm M}^z E^x}(\omega_{\rm p})$. The red arrows denote the growing resonance peaks with a smaller K_x.

We plot the behavior of the photocurrent conductivity $\sigma_{\rm w}(0;\omega_{\rm p})-\sigma_{\rm wo}(0;\omega_{\rm p})$ under the change of the resonance frequency in FIG. 4(a). In this calculation, we set the chemical potential as $\mu=\mu_2$ corresponding to the energy level at the upper Dirac point to discuss the resonance frequency dependence of the photocurrent generation from the localized spin dynamics above the optical gap of the electronic system. In FIG. 4(a), the peak structure of the photocurrent conductivity $\sigma_{\rm w}(0;\omega_{\rm p})-\sigma_{\rm wo}(0;\omega_{\rm p})$ shifts to a lower frequency as the magnetic anisotropy K_x gets smaller. The amplitude of the peaks of $\sigma_{\rm w}(0;\omega_{\rm p})-\sigma_{\rm wo}(0;\omega_{\rm p})$ exhibit the divergent behavior in the low-frequency regime.

Here, we discuss the low-frequency divergence of the injection current by counting the power of the photon frequency. Since the δ-function has dimension of $\omega_{\rm p}^{-1}$, Δ^{μ}_{ab} has dimension of $\omega_{\rm p}/k$, ξ^{μ}_{ab} has dimension of k^{-1}, and σ^{μ}_{ab} has no dimension, the scaling behavior of the injection current conductivities in Eq. (10) is given by

$$\sigma^{\mu;\nu\lambda}_{EE;\rm Inj}\sim\frac{\tau}{\omega_{\rm p}},\sigma^{\mu;\nu\lambda}_{{\rm S}E;\rm Inj}\sim\tau,\sigma^{\mu;\nu\lambda}_{\rm SS;Inj}\sim\tau\omega^{1}_{\rm p}, \qquad (11)$$

where $\sigma^{\mu;\nu\lambda}_{EE;\rm Inj}$ is the injection current originating from the electric field, $\sigma^{\mu;\nu\lambda}_{{\rm S}E;\rm Inj}$ comes from the interference effect between the electric field and the localized spin dynamics, and $\sigma^{\mu;\nu\lambda}_{\rm SS;Inj}$ is generated from the localized spin dynamics. Here, we use $k\sim\omega_{\rm p}$ owing to the linear dispersion of the Dirac electrons. This result of the power-counting analysis is consistent with the analytical expression of the injection current in SM [46]. Consequently, the injection current originating from the localized spin dynamics in Eq. (10) does not diverge in the low-frequency regime.

Next, we analyze the behavior of the electromagnetic susceptibility of the localized spin system in the low-frequency regime. We show the K_x-dependence of the electromagnetic susceptibility of the optically active

mode in FIG. 4(b),(c). The amplitude of the electromagnetic susceptibility gets larger as the resonance frequency shifts to a lower value. Even though the injection current conductivity $\sigma^{\mu;\nu\lambda}_{\mathrm{Inj;S}E}, \sigma^{\mu;\nu\lambda}_{\mathrm{Inj;SS}}$ in Eq. (10) does not show the low-frequency divergence, the photocurrent response arising from the localized spin dynamics in Eq. (8) diverges in the low-frequency regime owing to the low-frequency divergence of the resonance peak amplitude of the electromagnetic susceptibility.

Summary— In this study, we investigated the photocurrent generation from spin dynamics in AFM Dirac semimetals. First, we found that the photocurrent response is significantly enhanced by the localized spin dynamics due to the comparable energy scales of the electronic and localized spin systems. Second, we examined the μ-dependence of the photocurrent response. The photocurrent induced by localized spin dynamics exhibits distinct behaviors reflecting the presence of the Dirac point, which results in a sizable photocurrent generation when the electronic filling is set around the Dirac points. Finally, we discussed the low-frequency divergence of the photocurrent response driven by spin dynamics. We revealed that the photocurrent arising from spin dynamics diverges as the resonance frequency of the localized spin system shifts to a lower value. These effects can be observed in electrically switchable AFM Dirac semimetals such as CuMnAs [37, 38, 42, 47, 48].

Acknowledgement— K.H. thanks M. Sato for helpful discussion. This work is supported by Grant-in-Aid for Scientific Research from JSPS, KAKENHI Grant No. JP23K13058 (H.W.), No. JP24K00581 (H.W.), No. JP25H02115 (H.W.), No. 21H04990 (R.A.), JST-CREST No. JPMJCR23O4(R.A.), No. 25H01246 (R.A.), No. 25H01252 (R.A.), JST-ASPIRE No. JPMJAP2317 (R.A.), JST-Mirai No. JPMJMI20A1 (R.A.), JST SPRING, Grant Number JPMJSP2108 (K.H.). K.H. was supported by the Program for Leading Graduate Schools (MERIT-WINGS). This work was supported by the RIKEN TRIP initiative (RIKEN Quantum, Advanced General Intelligence for Science Program, Many-body Electron Systems).

* hattori-kohei053@g.ecc.u-tokyo.ac.jp
† hikaru-watanabe@g.ecc.u-tokyo.ac.jp

[1] V. I. Belinicher and B. I. Sturman, The photogalvanic effect in media lacking a center of symmetry, Soviet Physics Uspekhi **23**, 199 (1980).
[2] R. von Baltz and W. Kraut, Theory of the bulk photovoltaic effect in pure crystals, Physical Review B **23**, 5590 (1981).
[3] J. E. Sipe and A. I. Shkrebtii, Second-order optical response in semiconductors, Physical Review B **61**, 5337 (2000).
[4] N. Nagaosa, T. Morimoto, and Y. Tokura, Transport, magnetic and optical properties of weyl materials, Nature Reviews Materials **5**, 621 (2020).
[5] J. Liu, F. Xia, D. Xiao, F. J. García de Abajo, and D. Sun, Semimetals for high-performance photodetection, Nature Materials **19**, 830 (2020).
[6] F. de Juan, A. G. Grushin, T. Morimoto, and J. E. Moore, Quantized circular photogalvanic effect in weyl semimetals, Nature Communications **8**, 15995 (2017).
[7] F. de Juan, Y. Zhang, T. Morimoto, Y. Sun, J. E. Moore, and A. G. Grushin, Difference frequency generation in topological semimetals, Physical Review Research **2**, 012017 (2020).
[8] C.-K. Chan, N. H. Lindner, G. Refael, and P. A. Lee, Photocurrents in weyl semimetals, Physical Review B **95**, 041104 (2017).
[9] J. Ahn, G.-Y. Guo, and N. Nagaosa, Low-frequency divergence and quantum geometry of the bulk photovoltaic effect in topological semimetals, Physical Review X **10**, 041041 (2020).
[10] H. Watanabe and Y. Yanase, Chiral photocurrent in parity-violating magnet and enhanced response in topological antiferromagnet, Physical Review X **11**, 011001 (2021).
[11] Y. Ikeda, S. Kitamura, and T. Morimoto, Photocurrent induced by a bicircular light drive in centrosymmetric systems, Physical Review Letters **131**, 096301 (2023).
[12] Y. Ikeda, S. Kitamura, and T. Morimoto, Controllable photocurrent generation in dirac systems with two frequency drives, Physical Review B **110**, 235206 (2024).
[13] L. Wu, S. Patankar, T. Morimoto, N. L. Nair, E. Thewalt, A. Little, J. G. Analytis, J. E. Moore, and J. Orenstein, Giant anisotropic nonlinear optical response in transition metal monopnictide weyl semimetals, Nature Physics **13**, 350 (2017).
[14] J. Ma, Q. Gu, Y. Liu, J. Lai, P. Yu, X. Zhuo, Z. Liu, J.-H. Chen, J. Feng, and D. Sun, Nonlinear photoresponse of type-ii weyl semimetals, Nature Materials **18**, 476 (2019).
[15] G. B. Osterhoudt, L. K. Diebel, M. J. Gray, X. Yang, J. Stanco, X. Huang, B. Shen, N. Ni, P. J. W. Moll, Y. Ran, and K. S. Burch, Colossal mid-infrared bulk photovoltaic effect in a type-i weyl semimetal, Nature Materials **18**, 471 (2019).
[16] T. Morimoto and N. Nagaosa, Topological aspects of nonlinear excitonic processes in noncentrosymmetric crystals, Physical Review B **94**, 035117 (2016).
[17] T. Morimoto and N. Nagaosa, Shift current from electromagnon excitations in multiferroics, Physical Review B **100**, 235138 (2019).
[18] T. Morimoto, S. Kitamura, and S. Okumura, Electric polarization and nonlinear optical effects in noncentrosymmetric magnets, Physical Review B **104**, 075139 (2021).
[19] R. Toshio and N. Kawakami, Plasmonic quantum nonlinear hall effect in noncentrosymmetric two-dimensional materials, Physical Review B **106**, L201301 (2022).
[20] T. Morimoto and N. Nagaosa, Direct current generation by dielectric loss in ferroelectrics, Physical Review B **110**, 045129 (2024).
[21] Y.-H. Chan, D. Y. Qiu, F. H. da Jornada, and S. G. Louie, Giant exciton-enhanced shift currents and direct current conduction with subbandgap photo excitations produced by many-electron interactions, Proceedings of the National Academy of Sciences **118**, e1906938118 (2021).
[22] T. Kaneko, Z. Sun, Y. Murakami, D. Golež, and A. J. Millis, Bulk photovoltaic effect driven by collective exci-

tations in a correlated insulator, Physical Review Letters **127**, 127402 (2021).

[23] J. Iguchi, H. Watanabe, Y. Murakami, T. Nomoto, and R. Arita, Bulk photovoltaic effect in antiferromagnet: Role of collective spin dynamics, Physical Review B **109**, 064407 (2024).

[24] K. Hattori, H. Watanabe, and R. Arita, Nonlinear hall effect driven by spin-charge-coupled motive force (2025), arXiv:2501.11234 [cond-mat.str-el].

[25] M. Sotome, M. Nakamura, J. Fujioka, M. Ogino, Y. Kaneko, T. Morimoto, Y. Zhang, M. Kawasaki, N. Nagaosa, Y. Tokura, and N. Ogawa, Spectral dynamics of shift current in ferroelectric semiconductor sbsi, Proceedings of the National Academy of Sciences **116**, 1929 (2019).

[26] M. Sotome, M. Nakamura, T. Morimoto, Y. Zhang, G.-Y. Guo, M. Kawasaki, N. Nagaosa, Y. Tokura, and N. Ogawa, Terahertz emission spectroscopy of ultrafast exciton shift current in the noncentrosymmetric semiconductor cds, Physical Review B **103**, L241111 (2021).

[27] M. Nakamura, Y.-H. Chan, T. Yasunami, Y.-S. Huang, G.-Y. Guo, Y. Hu, N. Ogawa, Y. Chiew, X. Yu, T. Morimoto, N. Nagaosa, Y. Tokura, and M. Kawasaki, Strongly enhanced shift current at exciton resonances in a noncentrosymmetric wide-gap semiconductor, Nature Communications **15**, 9672 (2024).

[28] Y. Okamura, T. Morimoto, N. Ogawa, Y. Kaneko, G.-Y. Guo, M. Nakamura, M. Kawasaki, N. Nagaosa, Y. Tokura, and Y. Takahashi, Photovoltaic effect by soft phonon excitation, Proceedings of the National Academy of Sciences **119**, 10.1073/pnas.2122313119 (2022).

[29] M. Ogino, Y. Okamura, K. Fujiwara, T. Morimoto, N. Nagaosa, Y. Kaneko, Y. Tokura, and Y. Takahashi, Terahertz photon to dc current conversion via magnetic excitations of multiferroics, Nature Communications **15**, 4699 (2024).

[30] T. Jungwirth, X. Marti, P. Wadley, and J. Wunderlich, Antiferromagnetic spintronics, Nature Nanotechnology **11**, 231 (2016).

[31] V. Baltz, A. Manchon, M. Tsoi, T. Moriyama, T. Ono, and Y. Tserkovnyak, Antiferromagnetic spintronics, Review of Modern Physics **90**, 015005 (2018).

[32] A. Manchon, J. Železný, I. M. Miron, T. Jungwirth, J. Sinova, A. Thiaville, K. Garello, and P. Gambardella, Current-induced spin-orbit torques in ferromagnetic and antiferromagnetic systems, Review of Modern Physics **91**, 035004 (2019).

[33] L. S. Levitov, Y. V. Nazarov, and G. M. Eliashberg, Magnetoelectric effects in conductors with mirror isomer symmetry, Soviet Journal of Experimental and Theoretical Physics **61**, 133 (1985).

[34] V. Edelstein, Spin polarization of conduction electrons induced by electric current in two-dimensional asymmetric electron systems, Solid State Communications **73**, 233 (1990).

[35] Y. Yanase, Magneto-electric effect in three-dimensional coupled zigzag chains, Journal of the Physical Society of Japan **83**, 014703 (2014).

[36] J. Železný, H. Gao, K. Výborný, J. Zemen, J. Mašek, A. Manchon, J. Wunderlich, J. Sinova, and T. Jungwirth, Relativistic néel-order fields induced by electrical current in antiferromagnets, Physical Review Letter **113**, 157201 (2014).

[37] P. Wadley, B. Howells, J. Železný, C. Andrews, V. Hills, R. P. Campion, V. Novák, K. Olejník, F. Maccherozzi, S. S. Dhesi, S. Y. Martin, T. Wagner, J. Wunderlich, F. Freimuth, Y. Mokrousov, J. Kuneš, J. S. Chauhan, M. J. Grzybowski, A. W. Rushforth, K. W. Edmonds, B. L. Gallagher, and T. Jungwirth, Electrical switching of an antiferromagnet, Science **351**, 587 (2016).

[38] J. Godinho, H. Reichlová, D. Kriegner, V. Novák, K. Olejník, Z. Kašpar, Z. Šobáň, P. Wadley, R. P. Campion, R. M. Otxoa, P. E. Roy, J. Železný, T. Jungwirth, and J. Wunderlich, Electrically induced and detected néel vector reversal in a collinear antiferromagnet, Nature Communications **9**, 4686 (2018).

[39] A. Ono and S. Ishihara, Ultrafast reorientation of the néel vector in antiferromagnetic dirac semimetals, npj Computational Materials **7**, 171 (2021).

[40] A. Ono and Y. Akagi, Photocontrol of spin scalar chirality in centrosymmetric itinerant magnets, Physical Review B **108**, L100407 (2023).

[41] K. Hattori, H. Watanabe, J. Iguchi, T. Nomoto, and R. Arita, Effect of collective spin excitations on electronic transport in topological spin textures, Physical Review B **110**, 014425 (2024).

[42] L. Šmejkal, J. Železný, J. Sinova, and T. Jungwirth, Electric control of dirac quasiparticles by spin-orbit torque in an antiferromagnet, Physical Review Letters **118**, 106402 (2017).

[43] C. Aversa and J. E. Sipe, Nonlinear optical susceptibilities of semiconductors: Results with a length-gauge analysis, Physical Review B **52**, 14636 (1995).

[44] B.-J. Yang, T. A. Bojesen, T. Morimoto, and A. Furusaki, Topological semimetals protected by off-centered symmetries in nonsymmorphic crystals, Physical Review B **95**, 075135 (2017).

[45] L. Yue and M. B. Gaarde, Introduction to theory of high-harmonic generation in solids: tutorial, Journal of the Optical Society of America B **39**, 535 (2022).

[46] See Supplemental Material.

[47] P. Tang, Q. Zhou, G. Xu, and S.-C. Zhang, Dirac fermions in an antiferromagnetic semimetal, Nature Physics **12**, 1100 (2016).

[48] A. G. Linn, P. Hao, K. N. Gordon, D. Narayan, B. S. Berggren, N. Speiser, S. Reimers, R. P. Campion, V. Novák, S. S. Dhesi, T. K. Kim, C. Cacho, L. Šmejkal, T. Jungwirth, J. D. Denlinger, P. Wadley, and D. S. Dessau, Experimental electronic structure of the electrically switchable antiferromagnet cumnas, npj Quantum Materials **8**, 19 (2023).